Investigations of the structure of $Na_2S + P_2S_5$ glassy electrolytes and its impact on Na^+ ionic conductivity through *ab initio* molecular dynamics

A. Dive[a], Ye Zhang[c], Yan Yao[c,d], S.W. Martin[b], S. Banerjee[a,*]

[a] *School of Mechanical and Materials Engineering, Washington State University, Pullman, WA 99164-2920, USA*
[b] *Department of Materials Science and Engineering, Iowa State University, Ames, IA 50011, USA*
[c] *Department of Electrical & Computer Engineering and Materials Science and Engineering Program, University of Houston, Houston, TX 77204, USA*
[d] *Texas Center for Superconductivity, University of Houston, Houston, TX 77204, USA*

ARTICLE INFO

ABSTRACT

Abundant sodium reserves make sodium ion batteries a promising technology for high energy density applications such as grid energy storage. Identifying solid electrolytes with superior room temperature Na^+ ion conductivity is critical for designing safe and high energy density batteries with enhanced rate capabilities. We evaluated sodium thiophosphates [x Na_2S + (100-x) P_2S_5], potential glassy solid electrolytes (GSEs), using *ab initio* molecular dynamics (MD) simulations. We investigated the change in the local structure of these glasses with Na_2S content. We also calculated the relative fractions of different structural units within local structure for different compositions and compared them with those observed from FTIR and NMR spectroscopy. We investigated the plausible reasons for presence of polysulfides that act as Na^+ ion trapping sites thereby reducing the Na^+ ion conductivity. We report the maximum room temperature Na^+ ion conductivity of $\sim 10^{-5}\,S\,cm^{-1}$ for the x = 75 composition. Overall, our calculations provide theoretical insights on the role of polysulfides and different structural units on the ionic conductivity of GSEs aiding in the design of high ionic conductivity GSEs.

1. Introduction

Limited lithium reserves [1] and ever-increasing energy demands have intensified the need for economical alternatives for lithium ion batteries (LIBs). The nearly 1500 times greater natural abundance of sodium than lithium makes sodium-based batteries [2–4] a promising alternative. Despite their lower energy density than LIBs, sodium ion batteries (SIBs) are substantially more economical for grid energy storage. As in LIBs, organic liquid electrolytes (OLEs) pose challenges related to safe operation for SIBs. Solid-state sodium ion batteries (SSIBs) obviate this issue and have therefore received significant attention [5–8] in the past few years. Developing solid electrolytes (SEs) with high room-temperature ionic conductivities and superior electrochemical stability is critical to the success of SSIBs. Several studies have attempted to develop solid-state electrolytes (SSEs) [9–14], both crystalline and amorphous, with superior ionic conductivity and electrochemical stability. Recent measurements have shown that certain amorphous solids [15] such as glasses possess higher ionic conductivities than crystalline SEs. The enhanced ionic conductivities have been attributed to the larger available free volume due to the presence of disordered short-range order (SRO) and medium range order (MRO)

structures in these glassy solid electrolytes (GSEs) [16–18].

Sulfide glasses [19–24] have superior ionic conductivities ($\sim 10^{-2}\,S\,cm^{-1}$ [25]) at room temperature compared to the oxide glasses that have ionic conductivities at the very highest of $\sim 10^{-6}\,S\,cm^{-1}$ at room temperature. Also, sulfide glasses are more favorable due to their low synthesis temperatures and low grain boundary resistances [26–29]. For example, Hayashi et al. [30] have reported that the ionic conductivity of Na_3PS_4 glass ceramics (GCs) is ~ 0.2 mS cm^{-1} at 25 °C. Since then, several research efforts have attempted to improve the ionic conductivity of the Na_3PS_4 GCs through doping [31–33] or forming composite GCs [34–36]. Despite their high ionic conductivity, these GCs have higher processing costs because of additional heat treatment as compared to pure GSEs. The ionic conductivity of pure GSEs can be improved by using mixed glass formers (MGF) leveraging the mixed glass former effect (MGFE) [37–40]. Bischoff et al. [41] reported the effects of the MGF on the structures in and the ionic conductivities of yNa_2S + $(1–y)$ [x GeS_2 + $(1-x)$ $PS_{5/2}$] glasses. They reported a negative MGFE for $0.50\,Na_2S$ + 0.50 [x GeS_2 + $(1-x)$ $PS_{5/2}$] ternary GSE due to presence of P^0 structural units that act as Na^+ ion trapping sites. Here, the superscript indicates the number of bridging sulfurs (BSs) that covalently bond two P atoms to each other. Likewise,

---

Watson et al. [42] studied the effects of MGF on the structures in and the ionic conductivities of 0.50 Na_2S + 0.50 [x SiS_2 + (1-x) $PS_{5/2}$] and 0.67 Na_2S + 0.33 [x SiS_2 + (1-x) $PS_{5/2}$] GSEs. They also report a negative MGFE in both glass compositional series like that reported by Bischoff et al. [41]. These reports provide some insight about the MGFEs in these ternary GSEs, but a detailed understanding of the local structures and their subsequent impacts on the ionic conductivity of these GSEs are still largely open questions and yet are essential for design of new GSEs.

In our previous study [43], we have extensively modeled and analyzed the structure of x Na_2S + (100-x) SiS_2 GSEs using atomistic simulations. These calculations, based on molecular dynamics (MD) methods, were able to relate the local structure of GSEs to their ionic conductivity. In the present study, we employed *ab initio* molecular dynamics (aiMD), which performs quantum calculations to determine the atomistic interactions and simulates the dynamics at finite temperatures, to analyze the local structures of binary x Na_2S + (100-x) P_2S_5 glasses and correlate them to the Na^+ ion migration. Understanding the local structure and ion migration in these binary GSEs would be an advancement towards modeling more complex, and in some case higher conducting, ternary GSEs, such as x Na_2S + (100-x) [y SiS_2 + (1-y) $PS_{5/2}$] and x Na_2S + (100-x) [y GeS_2 + (1-y) $PS_{5/2}$] described above. Bischoff et al. [44] have extensively characterized x Na_2S + (100-x) P_2S_5 glasses using NMR and Raman spectroscopy, but have not addressed the impact of the local SRO structure on the ionic conductivity of these glasses. Similarly, Watson et al. [42] reported the presence of polysulfides, ^{-1}S-S_n-S^{-1}, in 0.50 Na_2S + 0.50 [x SiS_2 + (1-x) $PS_{5/2}$] GSEs using Raman spectroscopy, but do not provide any insights about the formation of these polysulfides in these GSEs. In the present work, we have investigated a range of x Na_2S + (100-x) P_2S_5 glasses to analyze the changes in the local structure and investigate the mechanisms leading to formation of polysulfides in x Na_2S + (100-x) P_2S_5.

The P−S bond in these GSEs show a resonant behavior [44] that cannot be accurately modeled with classical MD methods due to the unavailability of empirical forcefields that account for polarization effects and resonant structures in these chemical bonds. Hence, we employed aiMD simulation methods to more accurately model these x Na_2S + (100-x) P_2S_5 GSEs. We calculated the relative fractions of the different SRO structural units present in the GSEs for a range of compositions, x, to understand the impact of the Na_2S content on the relative fractions of these SRO units. Since polysulfides are known to reduce ionic conductivity, we investigated the possible mechanisms leading to formation of polysulfides in these GSEs. Finally, we calculated the composition, x, dependence of the ionic conductivity of these GSEs at room temperature (25 °C) and attributed the trend to presence of various SRO structural units.

2. Methodology

We evaluated the local structure and Na^+ ion transport properties for x Na_2S + (100-x) P_2S_5 GSEs (33 ≤ x ≤ 75) using aiMD simulations through the QUICKSTEP [45] algorithm of the CP2K [46] package, employing the Gaussian and Augmented plane waves (GAPW) approach. We utilized Goedecker-Teter-Hutter (GTH) type basis sets, optimized for molecular calculations (MOLOPT) [47], along with GTH pseudopotentials [48] for the DFT calculations. The details of the pseudopotentials and corresponding basis sets are provided in Table 1. Here, DZVP and TZVP stand for double and triple zeta for valence electrons and polarizable basis sets, respectively. We selected the basis sets based on prior optimization study by Hutter et al. [47]. We selected an optimum energy cut-off of 550 Ry following an optimization study for this system.

The simulated GSE structure comprised of 144 ions in a domain of volume 3375 $Å^3$. We created a starting structure, with a density of 2 g/cc, as reported from experiments [44] to form the glasses using a

Table 1
Basis sets and pseudopotentials utilized for *ab initio* MD simulations are reported.

Sr. no	Ion type	Basis set	Pseudopotential
1	Na	DZVP-SR-MOLOPT-GTH	GTH-PBE-q9
2	P	TZVP-MOLOPT-GTH	GTH-PBE-q4
3	S	TZVP-MOLOPT-GTH	GTH-PBE-q6

standard melt-quench technique [49–51]. The melt-quench technique involves initial heating up of the system to a form a melt at 1500 K and holding the melt at this temperature for 10 ps to randomize the melt. We then quenched the melt to room temperature at a very high quenching rate of 10^{14} K/s [50]. We initially equilibrated the quenched glass at room temperature (300 K) under the NPT (constant number of atoms, pressure, and temperature) ensemble for 100 ps to achieve an equilibrium density. The system was then further equilibrated at 300 K under NVT (constant number of atoms, volume and temperature) ensemble for additional 100 ps to remove any residual stress during quenching. Finally, we analyzed all the structural and ion transport properties by analyzing the trajectories for production runs of the systems for 40 ps under NVT ensemble.

We have also performed geometrical optimization of the different SRO structural units using the same basis sets and pseudopotentials. We optimized the SRO structures until the force convergence criteria of 0.02 eV/Å were achieved.

The Synchrotron radiation scattering experiments were carried out at the beamline 11-ID-C (Advanced Photon Source, Argonne National Laboratory) using the X-ray of energy 105.70 keV (λ = 0.1173 Å). The scattered radiation was collected with a Perkin Elmer area detector in a symmetric transmission geometry. The Na_3PS_4 powder was sealed into the Kapton capillary to avoid air exposure and the obtained data was calibrated against a CeO_2 standard. To improve the statistical accuracy, five images were taken with the exposure time of 30 s per image. The obtained 2D patterns from multiple exposures were combined and integrated 1D data using the GSAS-II program. The overall reduced or differential pair distribution function (PDF) or G(r) in real space was obtained by Fourier-transformation of the total scattering intensity, which is a function of the wave vector, Q.

We calculated the overall pair distribution function g(r) [52] from the individual pairwise radial distribution functions $g_{\alpha-\beta}(r)$. The details of the calculations can be found in Supplementary Information. The overall reduced or differential pair distribution functions [53] G(r) were calculated using Eq. (1):

$$G(r) = 4\pi r \rho_0 [g(r) - 1] \tag{1}$$

where, g(r) is the overall pair distribution function and ρ_0 is the number density of the atoms in the glass.

3. Results and discussions

3.1. Validation

The density of the 75 Na_2S + 25 P_2S_5 GSE calculated from aiMD is 1.87 g/cc and compares very well to the experimentally [44] measured density of 1.89 g/cc. The density matches closely providing an initial validation of the structure in aiMD. Fig. 1 compares the calculated $G(r)$ from aiMD to that obtained from neutron scattering experiments for the same 75 Na_2S + 25 P_2S_5 glass. The $G(r)$ plot obtained from aiMD shows very good agreement with that obtained from neutron scattering further validating the aiMD simulations. The first peak in Fig. 1 at ~2.1 Å corresponds primarily to P−S bonds within the PS_4 tetrahedral chain SRO units present in the glass. The second peak at ~2.8 Å corresponds to the Na^+ ions bonded to non-bridging sulfur (NBS) ions (S^-). The third major peak at ~3.5 Å corresponds to the S−S distances in the PS_4 tetrahedron.
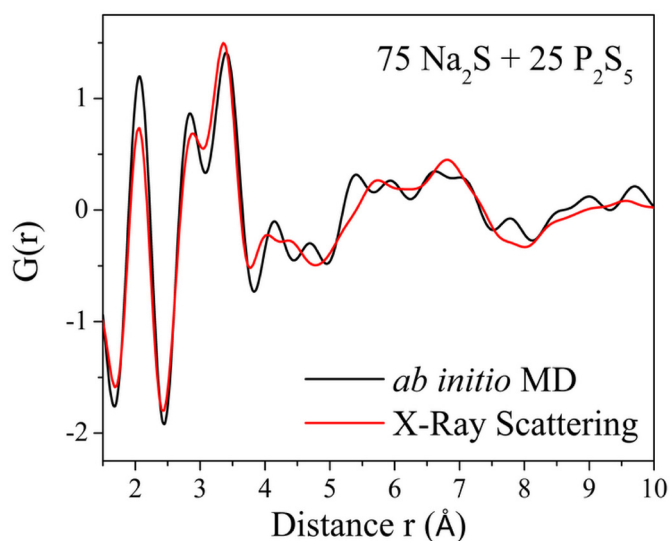
Fig. 1. Overall reduced pair distribution function $G(r)$ plots calculated from aiMD and neutron scattering experiments for 75 Na_2S + 25 P_2S_5 GSE.

3.2. Impact of Na_2S concentration on local SRO structure of the GSEs and their Na^+ conductivities

We modeled four different glass compositions and Table 2 shows the compositions and densities of these glasses as calculated from aiMD simulations.

Na_2S is called a glass modifier [54] because it breaks down the continuous chains of P–S tetrahedra by forming terminating ionic ≡P–$S^{-1}Na^+$ NBS bonds. Therefore, increasing the Na_2S content leads to a decrease in the density of the GSE as observed from the calculated densities presented in Table 2. Breaking of the P–S tetrahedral chains could lead to formation of various other SRO structural units in the GSE thereby modifying the local structure.

Bischoff et al. [44] have determined the predominantly observed local SRO structural units in these x Na_2S + (100-x) P_2S_5 GSEs through a combination of FTIR, Raman, and ^{31}P magic angel spinning (MAS) NMR spectroscopies. Fig. 2 shows these commonly observed SRO structural units as reported by Bischoff et al. [44]. Each of these structural units has unique P–S, and P–P bonds. The $G(r)$ plots in Fig. 1 alone cannot characterize these different SRO structural units present in the glass. Furthermore, the $G(r)$ functions cannot distinguish between three different bond types (P–S, S–S and P–P) at ~2.1 Å arising from different structural units. Hence, we need to analyze the individual pairwise radial distribution functions ($g_{\alpha-\beta}(r)$) to characterize these different structural units in more detail.

The PS_4 tetrahedron is an integral part of majority of the SRO structural units presented in Fig. 2. The P=S can very easily be in resonance with the P–S^- bonds in these structural units. To confirm the resonance of P=S in the structural units, we performed DFT geometry optimization of these structural units in vacuum at 0 K. We calculated the P=S, P–S and P–S^- bond lengths from the optimized structures and these are shown in Table 3.

We have found that the P=S bond is completely resonating in

Table 2
Densities of the different x Na_2S + (100-x) P_2S_5 glasses at 300 K examined in this study.

Composition	Calculated density from aiMD (g/mL)
33 Na_2S + 67 P_2S_5	2.06
50 Na_2S + 50 P_2S_5	2.01
67 Na_2S + 33 P_2S_5	1.96
75 Na_2S + 25 P_2S_5	1.87

nature only in P^{1P} and P^0 SRO structural units as evident from Table 3. For the structural units P^2, $P^{2'}$, P^1 the P=S bond resonates only with the P–S^-, where the S^- is an NBS ion. For the structural units $P^{:3}$ and $P^{:0}$, no P=S is present. Table 3 also reports the P–P distance in different DFT optimized SRO structural units. The calculated equilibrium bond lengths and distances between P–S and P–P within these structural units will be referred to in the subsequent sections and help determine the local structures. More details about the P–S bond resonant behavior are reported in Supplementary Information.

We calculated the relative fractions of these reported SRO structural units shown in Fig. 2 using an in-house developed code. The structural units are reported as atomic percentages of the total P atoms present in the glass. Table 4 shows the relative fractions of these structural units for the different glass compositions.

The percentages in brackets are the relative fractions of these structural units calculated from NMR experiments by Bischoff et al. [44]. Overall, the comparisons show that aiMD can accurately capture the major SRO structural units reported by Bischoff et al. in their NMR data reported in Table 4. The individual pairwise $g_{\alpha-\beta}(r)$ plots coupled with the relative fractions reported in Table 4 can now be used to more precisely characterize the local structure of these glasses. Table 4 shows that the relative fraction of P^3, $P^{:3}$ and P^2 units decrease with increase in Na_2S content. This is in accordance with the fact that Na_2S being a glass modifier breaks down the continuous PS_4 chains. To understand the change in the relative fractions more clearly with respect to these different structural units, we calculated radial pair distribution function plots ($g_{P-P}(r)$) between P–P atoms for all compositions. Fig. 3 shows the $g_{P-P}(r)$ plot for different compositions.

For the 33 Na_2S + 67 P_2S_5 GSE, Table 4 reports that $P^{:3}$, P^2 and P^{1P} units dominate the local structure. The P^3, $P^{:3}$ and P^2 SRO structural units form the continuous P–S tetrahedral chains in the glasses because of the presence of bridging sulfurs (BSs). In Fig. 3, a small peak at ~3.0 Å corresponds to the P–P distance in a P^3 SRO structural unit. The presence of a lone pair of electrons in $P^{:3}$ and one NBS ion on the P_2 SRO units leads to an increase in the P–P distance in these SRO structural units. Hence, we observe a second major peak at ~3.4 Å corresponding to the P–P distance in $P^{:3}$ and P^2 units. The first major peak at 2.2 Å corresponds to the P–P bond length in the P^{1P} SRO structural unit.

With an increase in the Na_2S concentration, the P–S chains break down through the formation of more NBSs and the concentration of NBSs increases as evident from the increase in P^2 units for 50 Na_2S + 50 P_2S_5 GSE reported in Table 4. The P^3 units disappear completely and hence no peaks are observed at ~3.0 Å in Fig. 3. The increase in the relative fraction of P^2 units, lead to a slight shift of the second major peak at ~3.5 Å. Also, as the concentration of P^{1P} units decreases, the intensity of the first major peak decreases in Fig. 3.

With further increase in Na_2S content, the P–S tetrahedral chains are completely broken off into separate discrete molecular anion species in the 67 Na_2S + 33 P_2S_5 GSE and hence the relative fractions of P^3, $P^{:3}$ and P^2 units is negligible. The $g_{P-P}(r)$ plots in Fig. 3 therefore exhibit a broad peak at ~3.5–3.8 Å arising from the P–P distance in P^1 and P^0 SRO structural units. The P–P distance of ~3.5 Å arises from the P^1 unit, whereas the P–P distance between the randomly distributed P^0 units leads to P–P distance > 3.5 Å. The intensity of the P–P peak at ~2.2 Å decreases due to the decrease in the P^{1P} concentration.

For 75 Na_2S + 25 P_2S_5 GSE, the P^0 units are predominantly present along with small amounts of P^{1P}, P^1 and $P^{:0}$ SRO structural units. Fig. 3 shows two peaks, the first one at ~3.5 Å arising from the presence of P^1 structural units in the glass. The second peak at ~3.6 Å arises from the P–P distance between randomly distributed P^0 structural units. The concentration of P^0 units in 75 Na_2S + 25 P_2S_5 glass is much higher than that for the 67 Na_2S + 33 P_2S_5 GSE and hence this second peak at ~3.6 Å is much sharper when compared to same peak for 67 Na_2S + 33 P_2S_5 glass in Fig. 3.

The structural analysis by Bischoff et al. [44] does not report the presence of any polysulfides within these glass compositions. However,
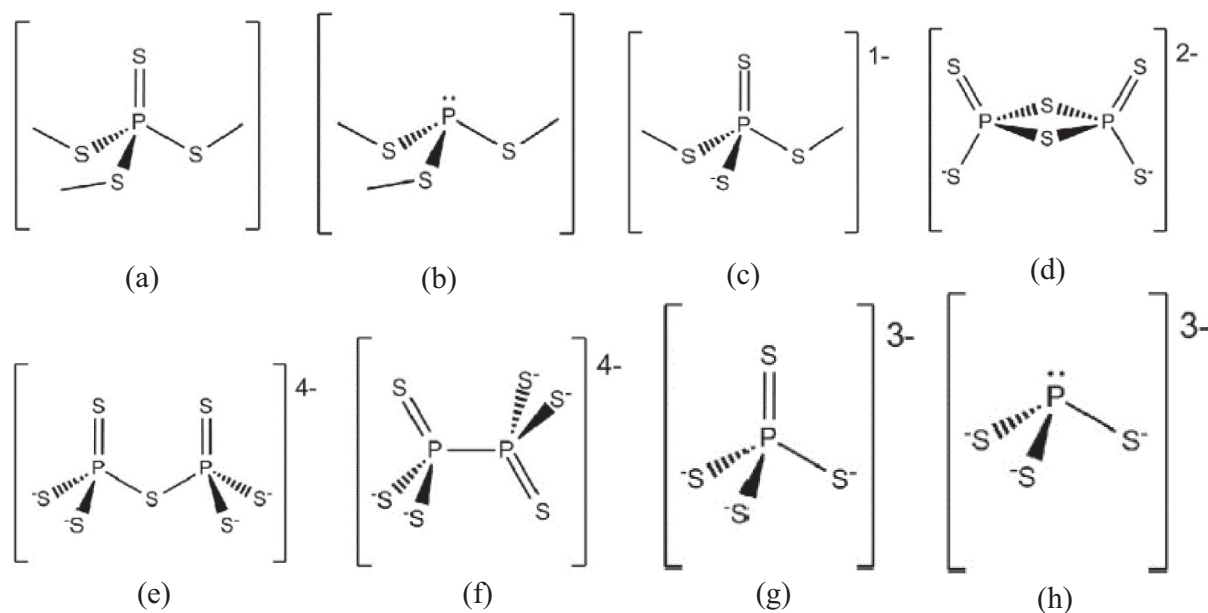
Fig. 2. (a) P^3, (b) $P^{:3}$, (c) P^2, (d) $P^{2'}$, (e) P^1, (f) P^{1P}, (g) P^0 and (h) $P^{:0}$ SRO units present in the x Na_2S + (100-x) P_2S_5 GSEs as reported by Bischoff et al. [44]. "Reprinted from Journal of Non-Crystalline Solids, 358(23), Christian Bischoff, Katherine Schuller, Michael Haynes, Steve W. Martin, Structural investigations of y Na_2S + (1−y) $PS_{5/2}$ glasses using Raman and infrared spectroscopies, 3216-3222, Copyright (2012), with permission from Elsevier."

the structural units, $P^{:3}$, P^{1P} and $P^{:0}$ are all sulfur deficient, which could lead to presence of free sulfur in the local structure of these glasses. These free sulfur ions could easily form polysulfides, ^{-1}S-S_n-S^{-1}, type structural units. Formation of polysulfides can potentially impact ion conductivity and therefore needs to be considered and analyzed in detail. To verify this hypothesis, we calculated the individual $g_{S-S}(r)$ plots for S—S ion pairs from the aiMD simulations and the results are shown in Fig. 4. Fig. 4 shows two major peaks for $g_{S-S}(r)$, one at ~2.1 Å and the other at ~3.3 Å. The first peak at ~2.1 Å arises from the presence of S—S bonds in the polysulfides, ^{-1}S-S_n-S^{-1}, units present in the glass, whereas the second peak at ~3.3 A arises from the S—S distance between the S ions within the PS_4 tetrahedral units as reported in Fig. 2. The concentration of polysulfides is found to decrease with increase in the Na_2S content as observed in Fig. 4.

Based on the observed peak at ~2.1 Å in Fig. 4, we further calculated the relative fractions of polysulfides present in these GSEs with 2.1 Å specified as the cutoff S—S bond distance. Table 5 presents the relative fractions of polysulfides. The calculations confirm that the concentration of polysulfides decreases with increase in the concentration of Na_2S. This decrease in the concentration of polysulfides with increasing Na_2S content is consistent with the decrease in defect SRO units such as $P^{:3}$, P^{1P} and $P^{:0}$.

Polysulfides can act as Na^+ ion trapping sites and lower the Na^+ ionic conductivity in these GSEs. Therefore, it is important to investigate the plausible reasons leading to formation of polysulfides and

Table 4

Relative fractions of the SRO structural units present in x Na_2S + (100-x) P_2S_5 GSEs. The experimentally measured fractions, taken from ref. [44]. wherever applicable, are shown in bold in parentheses.

Type of structural unit	Relative fractions			
	33 Na_2S + 67 P_2S_5	50 Na_2S + 50 P_2S_5	67 Na_2S + 33 P_2S_5	75 Na_2S + 25 P_2S_5
P^3	3%	0%	0%	0%
$P^{:3}$	31%	14% **(5%)**	6% **(4%)**	5.5% **(3%)**
P^2	28%	64% **(90%)**	0%	0%
$P^{2'}$	0%	4%	0%	0%
P^1	0%	0 **(5%)**	58% **(68%)**	11% **(18%)**
P^{1P}	26%	15%	9% **(19%)**	11% **(9%)**
P^0	3%	3%	22% **(9%)**	67% **(70%)**
$P^{:0}$	9%	0%	5%	5.5%

therefore to use this understanding to reduce the content of polysulfides in these GSEs. Based on the general hypothesis that polysulfides can form in presence of free sulfur, we investigated the presence of free sulfur in these GSEs. As described above, Na_2S is a glass modifier and leads to the breaking of the P—S tetrahedral chains in the glass to form more depolymerized, fewer BSs and more NBSs, SRO structural units as shown in Fig. 2. The $P^{:3}$ and $P^{:0}$ structural units with a lone pair of electrons on P are sulfur deficient units that can lead to formation of

Table 3

Different P—S bond lengths in optimized structural units are shown.

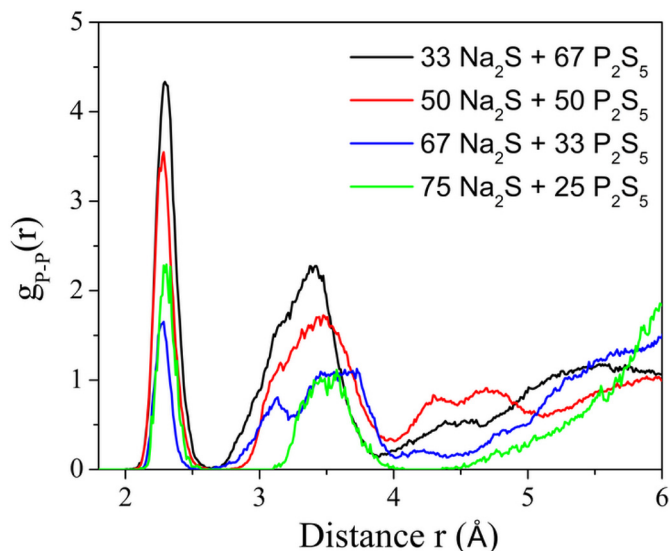| Type of structural unit	Bond lengths				Resonance information
	P = S	P-S	P-S⁻	P-P	
P^3	1.93	2.13	–	3.12	P = S is non-resonating
$P^{:3}$	–	2.15	–	3.52	No P=S bond
P^2	1.98	2.19	1.98	3.45	P = S is a resonating bond with P—S⁻ bond
$P^{2'}$	1.98	2.19	1.98	3.04	P = S is a resonating bond with P—S⁻ bond
P^1	2.05	2.28	2.05	3.48	P = S is a resonating bond with P—S⁻ bond
P^{1P}	2.06	–	2.06	2.2	P = S is a resonating bond with all S atoms
P^0	2.10	–	2.10	–	P = S is a resonating bond with all S atoms
$P^{:0}$	–	–	2.20	–	No P=S bond

Fig. 3. $g_{P-P}(r)$ plot for P−P pairs from 1.8 Å to 5.0 Å is shown.

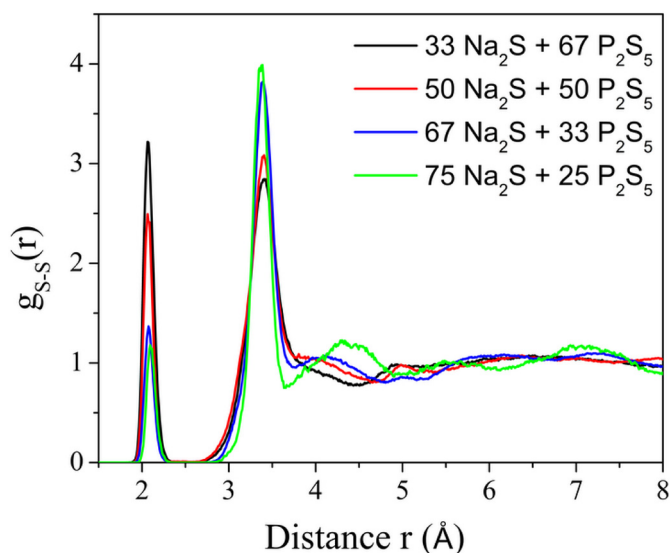**Fig. 4.** $g_{s-s}(r)$ plots from 1.5 Å to 8.0 Å for the S−S pairs.

Table 5

Relative fractions of polysulfides present in x Na$_2$S + (100-x) P$_2$S$_5$ GSEs.

Type of structural unit	Relative fractions			
	33 Na$_2$S + 67 P$_2$S$_5$	50 Na$_2$S + 50 P$_2$S$_5$	67 Na$_2$S + 33 P$_2$S$_5$	75 Na$_2$S + 25 P$_2$S$_5$
Polysulfides	21%	14%	9%	6%

free sulfur. The P^3 and P^0 units can easily undergo structural transformation to form these P$^{:3}$ and P$^{:0}$ structural units by losing one of the sulfur ions leading to generation of free sulfur. Also, the P^{1P} SRO structural unit is sulfur deficient with a P−P bond. The P^1 structural unit can easily transform into a P^{1P} unit by releasing a free sulfur ion. Hence, of all the different structural units, the presence of P$^{:3}$, P$^{:0}$ and P^{1P} structural units in the glass may lead to formation of free sulfur and ultimately the polysulfides.

However, the P$^{:0}$ structural unit can form through several distinct mechanisms. Firstly, a P^1 structural unit can disintegrate to form a P^0 and P$^{:0}$ unit. Secondly, the P$^{2'}$ structural units can disintegrate to form

Table 6

Enthalpies for different structural transformation reactions are reported.

Structural transformation	Enthalpy ($\Delta H = \Delta H_p - \Delta H_r$) kcal/mol
P$^3 \to$ P$^{:3}$ + S	−16.89
P$^0 \to$ P$^{:0}$ + S	+5.08
P$^1 \to$ P^{1P} + S	−10.02
P$^1 \to$ P^0 + P$^{:0}$	−66.40
P$^{2'} \to$ P$^{:0}$ + P$^{:0}$	−106.31

two P$^{:0}$ units. These two mechanisms, however, do not involve generation of any free sulfur. To obtain further insights into these different reactions, we calculated the enthalpies for different reactions leading to formation of free sulfur using DFT calculations. Table 6 shows the different structural transformations and their calculated enthalpies at 0 K.

Table 6 shows that the structural transformations of P$^{2'}$ and P^1 units to form P$^{:0}$ and P^0 units are highly favorable due to high negative enthalpies. These reactions do not lead to formation of free sulfur. However, the structural transformations of P^3 and P^1 to form P$^{:3}$ and P^{1P}, respectively, also have negative reaction energies that will make these reactions feasible during the glass formation. On the other hand, the structural transformation of P^0 to P$^{:0}$ has a positive reaction energy making it the least probable transformation. The above results show that the presence of these P$^{:3}$ and P^{1P} SRO structural units lead to formation of free sulfur and ultimately polysulfides. Table 4 shows high concentration of P$^{:3}$ and P^{1P} units in 33 Na$_2$S + 67 P$_2$S$_5$ glasses which leads to high polysulfide concentration. With increase in the Na$_2$S content, the concentration of P$^{:3}$ and P^{1P} units decreases and hence the concentration of polysulfides also decreases as reported in Tables 4 and 5. Hence, P$^{:3}$ and P^{1P} structural units are the major contributors to formation of polysulfides in the glasses.

Low concentration of polysulfides lead to improved Na$^+$ ionic conductivity since these polysulfides act as Na$^+$ ion trapping sites. However, Na$^+$ ionic conductivity is not solely dependent on the concentration of polysulfides. Other factors that can impact the Na$^+$ ionic conductivity are (i) the concentration of Na$^+$ ions and therefore available sites for ion hops and (ii) the activation energy for Na$^+$ ion hops. We calculated the ionic conductivity of these glasses from the self-diffusion coefficient D_0 of Na$^+$ ions based on

$$\sigma = \frac{Ne^2D_0}{Vk_BT} \tag{2}$$

where, N is the number of Na$^+$ ions in the volume V of the GSE, D_0 is the self-diffusion coefficient of Na$^+$ ions, T is 300 K and k_B is the Boltzmann constant. Table 7 reports the calculated ionic conductivities at 300 K.

The date presented in Table 7 indicates that the aiMD simulations overpredict the ionic conductivity of these glasses as compared to the experimentally reported values [57]. However, the simulations accurately capture the trend in ionic conductivity with Na$_2$S content. The ionic conductivity increases with increasing Na$_2$S content due to multiple reasons. Firstly, the concentration of polysulfides decreases with

Table 7

Calculated ionic conductivity of x Na$_2$S + (100-x) P$_2$S$_5$ glasses at 300 K are compared with experimental measurements by Nose et al. [57]. Experimental data was not available for 33 Na$_2$S + 67 P$_2$S$_5$ glass.

Composition	Ionic conductivity calculated from aiMD (S cm^{-1})	Ionic conductivity measured experimentally (S cm^{-1})
33 Na$_2$S + 67 P$_2$S$_5$	2.3×10^{-8}	−
50 Na$_2$S + 50 P$_2$S$_5$	7.5×10^{-7}	3.5×10^{-7}
67 Na$_2$S + 33 P$_2$S$_5$	4.2×10^{-6}	1.3×10^{-6}
75 Na$_2$S + 25 P$_2$S$_5$	1.2×10^{-5}	8.5×10^{-6}

Fig. 5. RDF plot for Na−Na pairs from 2.0 Å–10.0 Å is presented.

Table 8
Calculated theoretical energy barriers for Na$^+$ ion hops are reported.

Composition	λ_{cation} (Å)	G (GPa)	ε_r	ΔE_B (kJ/mol)	ΔE_S (kJ/mol)	ΔE_T (kJ/mol)
33 Na$_2$S + 67 P$_2$S$_5$	4.5	4.0	5.65	17.76	14.29	32.07
	5.3	4.0	5.65	19.41	16.83	36.24
50 Na$_2$S + 50 P$_2$S$_5$	4.6	5.5	8.97	11.33	19.65	30.97
67 Na$_2$S + 33 P$_2$S$_5$	4.0	7.0	15.63	6.01	22.23	28.24
75 Na$_2$S + 25 P$_2$S$_5$	3.5 (Primary)	7.1	23.5	3.68	15.65	19.33
	5.5 (Secondary)	7.1	23.5	4.62	23.26	27.88

Na$_2$S content as explained in detail earlier. Secondly, the concentration of Na$^+$ ions increases with increasing Na$_2$S which leads to higher ionic conductivity. The activation energy is directly correlated to the distance between Na$^+$ ion sites in the glass. The individual $g_{Na-Na}(r)$ plot can provide insights about the distance between Na$^+$ ions. Fig. 5 shows the individual $g_{Na-Na}(r)$ plot as calculated from aiMD simulations.

The $g_{Na-Na}(r)$ plot for 33 Na$_2$S + 67 P$_2$S$_5$ shows two peaks, one small peak at ~4.75 Å and a major peak at ~5.5 Å. The first peak at 4.75 Å arises from the Na−Na distance between the sodium ions coordinating with NBS ions in P^{1P} structural units. The second major peak at ~5.5 Å arises from the Na−Na distance between sodium ions coordinating with NBS ions in P^2 structural units. As the concentration of Na$_2$S increases, the first peak observed in 33 Na$_2$S + 67 P$_2$S$_5$ glass disappears due to decrease in the relative fraction of P^{1P} structural units. The second peak shifts to lower Na−Na distance due to increase in the number of NBS ions as well as the sodium ions in the glass. For 75 Na$_2$S + 25 P$_2$S$_5$ glass, we observe a small peak developing at ~5.5 Å. This new peak may be representative of secondary sites that the Na$^+$ ions can occupy.

To correlate the observed trend in ionic conductivity to the projected ion hop distances based on the RDFs in Fig. 5, we calculated the theoretical activation energy for Na$^+$ ion hops for all the four compositions using the modified Anderson-Stuart (AS) [55] and McElfresh-Howitt (MH) [56] models. The electrostatic binding energy (ΔE_B) in the AS model, is presented below in Eq. (3):

$$\Delta E_B = \frac{\beta Z_{anion} Z_{cation} e^2}{4\pi\varepsilon_0\varepsilon_r} \left(\frac{1}{r_{cation} + r_{anion}} \right) \quad (3)$$

Here, Z_{anion} and Z_{cation} are the partial charges on the anion and cation respectively, and r_{cation} and r_{anion} are the ionic radii of cation and anion respectively, ε_0 and ε_r are the dielectric permittivity of vacuum and glass respectively and β is a displacement factor. The displacement factor β is calculated from:

$$\beta = -1 + \left(\frac{2(r_{cation} + r_{anion})}{(\lambda_{anion})} \right) \quad (4)$$

where, λ_{anion} is the distance between the two anions across which the Na$^+$ ion hops. Based on the AS model, the value of λ_{anion} is equal to [$\lambda_{cation} + 2(r_{cation} + r_{anion})$].

The MH model expresses the corresponding strain binding energy (ΔE_S) as:

$$\Delta E_S = \pi G (r_{cation} - r_D)^2 \left(\frac{\lambda_{cation}}{2} \right) \quad (5)$$

Here, G is the shear modulus of the glass, r_D is the doorway radius for the Na$^+$ ion to move through from one site to another and λ_{cation} is the Na$^+$ ion hop distance. We selected the λ_{cation} from the corresponding Na−Na peaks in $g_{Na-Na}(r)$ plot. Nose et al. [57] have reported the values for shear modulus (G) for different compositions. We calculated the r_D based on a representative regular tetrahedral site occupied by Na$^+$ ion. Table 8 reports the calculated theoretical activation energy ($\Delta E_T = \Delta E_B + \Delta E_S$) based on the AS and MH models for all four compositions. We observe two Na−Na peaks for 33 Na$_2$S + 67 P$_2$S$_5$ glass at ~4.5 Å and ~5.3 Å in Fig. 5. To account for Na$^+$ ion hops across these two distinct sites, we calculated the activation energy corresponding to both these peaks as presented in Table 8. Likewise, in 75 Na$_2$S + 25 P$_2$S$_5$ glass, we observe the presence of primary and secondary Na$^+$ ion sites at ~3.5 Å and ~5.5 Å respectively. Table 8 therefore reports the activation energy for Na$^+$ ion hops across both these sites.

The theoretical calculations provide insights about the individual contributions from ΔE_B and ΔE_S to the total activation energy for ion hop at varying compositions. The overall trend, observed from the data presented in Table 8, indicates that the activation energy drops with increase in Na$_2$S concentration. The electrostatic binding energy ΔE_B is inversely proportional to ε_r of the glass, which is also evident from the results in Table 8. For a fixed glass composition, the ΔE_B value increases with increase in λ_{cation} as seen from the data presented for 33 Na$_2$S + 67 P$_2$S$_5$ and 75 Na$_2$S + 25 P$_2$S$_5$ glass. On the other hand, observed trends in ΔE_S is determined by the competing factors, the shear modulus G and the cation hop distance λ_{cation}. Like ΔE_B, the ΔE_S initially increases with increasing Na$_2$S concentration up until 67 Na$_2$S + 33 P$_2$S$_5$ due to the increase in the G of glass that plays a dominant role. However, ΔE_S is lower in 75 Na$_2$S + 25 P$_2$S$_5$ compared to 67 Na$_2$S + 33 P$_2$S$_5$ due to the decrease in λ_{cation} for the primary Na$^+$ sites at ~3.5 Å. In this case, λ_{cation} is the dominant parameter, since the increase in G is not significant. For a fixed glass composition, and therefore fixed shear modulus, the value of ΔE_S increases on increase in the λ_{cation} in accordance with Eq. (5). This trend is observed from the data for 33 Na$_2$S + 67 P$_2$S$_5$ and 75 Na$_2$S + 25 P$_2$S$_5$ glass reported in Table 8. It is noteworthy that the overall activation energy for Na$^+$ ion hops across the secondary sites for 75 Na$_2$S + 25 P$_2$S$_5$ glass is still lower than the respective activation energies for Na$^+$ ion hops for other compositions. Overall, the decrease in overall activation energy for Na$^+$ ion hops coupled with decrease in polysulfide concentration lead to the increase in ionic conductivity reported in Table 7. This trend is corroborated by the measurements of Nose et al. [57] that reported that the maximum ionic conductivity is attained in 75 Na$_2$S + 25 P$_2$S$_5$ glass and is ~8.5 × 10^{-6} S cm^{-1}.

4. Conclusions

We performed aiMD simulations to model x Na$_2$S + (100-x) P$_2$S$_5$ GSEs. The simulations were validated by comparing the reduced overall pair distribution function G(r) calculated from MD simulations to those obtained from x-ray scattering for 75 Na$_2$S + 25 P$_2$S$_5$ glass. We

calculated the relative fractions of different SRO structural units for a range of x Na_2S + (100-x) P_2S_5 glasses (33 ≤ x ≤ 75). Amongst these SRO units, we detected polysulfide species that act as Na^+ ion trapping sites and therefore lower ionic conductivity. Therefore, we investigated the formation of polysulfides in these glasses. P^{1P} and $P^{:3}$ SRO structural units are the major contributors to the formation of polysulfides. With increasing Na_2S concentration, the relative fractions of P^{1P} and $P^{:3}$ decreases resulting in lower polysulfide concentration. Ultimately, the ionic conductivity of glasses is determined by the activation energy for Na^+ ion hops across a range of sites. We calculated the activation energy for Na^+ ions for different compositions using theoretical models. The calculated activation energy decreases with increasing Na_2S content. Hence, the lowering of polysulfide concentration is augmented with decreasing activation energy for Na^+ ion hops and leads to improved ionic conductivity of these glasses with higher Na_2S content. We report a calculated maximum ionic conductivity of $1.2 \times 10^{-5}\,S\,cm^{-1}$ at 30 °C for 75 Na_2S + 25 P_2S_5 glass.

Acknowledgments

Appendix A. Supplementary data

Supplementary data to this article can be found online at https://doi.org/10.1016/j.ssi.2019.05.014.

References

[1] B. Dunn, H. Kamath, J.M. Tarascon, Electrical energy storage for the grid: a battery of choices, Materials for Grid Energy 334 (2011) 928.

[2] K. Vignarooban, R. Kushagra, A. Elango, P. Badami, B.E. Mellander, X. Xu, T.G. Tucker, C. Nam, A.M. Kannan, Current trends and future challenges of electrolytes for sodium-ion batteries, Intl. Jour. Of Hydrogen Energy 41 (2016) 2829.

[3] Z. Wen, Y. Hu, X. Wu, J. Han, Z. Gu, Main challenges for high performance NAS battery: materials and interfaces, Adv. Funct. Mater. 23 (2013) 1005.

[4] N. Yabuuchi, K. Kubota, M. Dahbi, S. Komaba, Research development on sodium-ion batteries, Chem. Rev. 114 (2014) 11636.

[5] K. Takada, Progress and prospective of solid-state lithium batteries, Acta Mater. 61 (2013) 759770.

[6] Y. Kato, S. Hori, T. Saito, K. Suzuki, M. Hirayama, A. Mitsui, M. Yonemura, H. Iba, R. Kanno, High-power all-solid-state batteries using sulfide superionic conductors, Nat. Energy 1 (2016) 16030.

[7] D.H. Kim, D.Y. Oh, K.H. Park, Y.E. Choi, Y.J. Nam, H.A. Lee, S.M. Lee, S.M. Lee, Y.S. Jung, Infiltration of solution-processable solid electrolytes into conventional Li-ion-battery electrodes for all-solid-state Li-ion batteries, Nano Lett. 17 (2017) 3013–3020.

[8] H. Gao, L. Xue, S. Xin, K. Park, J.B. Goodenough, A plastic-crystal electrolyte interphase for all-solid-state sodium batteries, Angew. Chem. Int. Edit. 56 (2017) 55415545.

[9] N. Anantharamulu, K.K. Rao, G. Rambabu, B.V. Kumar, V. Radha, M. Vithal, A wide ranging review on Nasicon type materials, J. Mater. Sci. 46 (2011) 2821–2837.

[10] Lu, F. Ciucci, Structural origin of the superionic Na conduction in $Na_2B_{10}H_{10}$ *closo*-borates and enhanced conductivity by Na deficiency for high performance solid electrolytes, J. Mater. Chem. A 4 (2016) 17740–17748.

[11] X. Lu, G. Xia, J.P. Lemmon, Z. Yang, Sodium-beta alumina batteries: status and challenges, J. Power Sources 195 (2010) 2431–2442.

[12] K.B. Hueso, M. Armand, T. Rojo, High temperature sodium batteries: status, challenges and future trends, Energy Environ. Sci. 6 (2013) 734–749.

[13] H.-P. Hong, Crystal structures and crystal chemistry in the system $Na_{1+x}Zr_2Si_xP_{3-x}O_{12}$, Mater. Res. Bull. 11 (1976) 173–182.

[14] A. Hooper, A study of the electrical properties of single-crystal and polycrystalline β-alumina using complex plane analysis, J. Phys. D. Appl. Phys. 10 (1977) 1487.

[15] C.A. Angell, Fast ion motion in glassy and amorphous materials, Solid State Ionics 9 (1983) 3–16.

[16] M. Tsutomu, Fast ion conducting glasses, Jour. of Non-Crys. Solids 73 (1985) 273–284.

[17] A. Dalvi, K. Shahi, Transport studies on mechanochemically synthesized amorphous $AgI–Ag_2O–CrO_3$ superionic system, Solid State Ionics 159 (2003) 369–379.

[18] K. Shahi, J.B. Wagner, Phase transition and the Ag^+-ion diffusion in AgI: effect of homovalent Br-ion substitution, Phy. Rev. B 23 (1981) 6417–6421.

[19] W. Yao, S.W. Martin, Ionic conductivity of glasses in the $MI + M_2S + (0.1Ga_2S_3 + 0.9GeS_2)$ system (M = Li, Na, K and Cs), Solid State Ionics 178 (2008) 1777.

[20] A. Hayashi, K. Noi, A. Sakuda, M. Tatsumisago, Superionic glass-ceramic electrolytes for room-temperature rechargeable sodium batteries, Nat. Commun. 3 (2012) 5.

[21] T. Minami, A. Hayashi, M. Tatsumisago, Recent progress of glass and glass-ceramics as solid electrolytes for lithium secondary batteries, Solid State Ionics 177 (2006) 2715–2720.

[22] J.H. Kennedy, Z. Zhang, H. Eckert, Ionically conductive sulfide-based lithium glasses, J. Non-Cryst. Solids 123 (1990) 328–338.

[23] N. Tanibata, K. Noi, A. Hayashi, M. Tatsumisago, Preparation and characterization of highly sodium ion conducting $Na_3PS_4–Na_4SiS_4$ solid electrolytes, RSC Adv. 4 (2014) 17120.

[24] F. Mizuno, A. Hayashi, K. Tadanaga, M. Tatsumisago, High lithium ion conducting glass-ceramics in the system $Li_2S-P_2S_5$, Solid State Ionics 177 (2006) 2721.

[25] Y. Seino, T. Ota, K. Takada, A. Hayashi, M. Tatsumisago, A sulfide lithium super ion conductor is superior to liquid ion conductors for use in rechargeable batteries, Energy Environ. Sci. 7 (2014) 627–631.

[26] M. Tatsumisago, A. Hayashi, Sulfide glass-ceramic electrolytes for all-solid-state lithium and sodium batteries, Int. J. Appl. Glas. Sci. 5 (2014) 226–235.

[27] I.H. Chu, H. Nguyen, S, H, Y.C. Lin, Z. Wang, Z. Xu, Z. Deng, Y.S. Meng, S.P. Ong, Room-temperature all-solid-state rechargeable sodium-ion batteries with a cl-doped Na_3PS_4 superionic conductor, ACS Appl. Mater. Interfaces 8 (2016) 7843–7853.

[28] N. Tanibata, K. Noi, A. Hayashi, M. Tatsumisago, Preparation and characterization of highly sodium ion conducting $Na_3PS_4–Na_4SiS_4$ solid electrolytes, RSC Adv. 4 (2014) 17120–17123.

[29] Y. Wang, W.D. Richards, S.P. Ong, L.J. Miara, J.C. Kim, Y. Mo, G. Ceder, Design principles for solid-state lithium superionic conductors, Nat. Mater. 14 (2015) 1026–1031.

[30] A. Hayashi, K. Noi, A. Sakuda, M. Tatsumisago, Superionic glass-ceramic electrolytes for room-temperature rechargeable sodium batteries, Nat. Commun. 3 (2012) 856.

[31] H. Huang, H.H. Wu, X. Wang, B. Huang, T.Y. Zhang, Enhancing sodium ionic conductivity in tetragonal-Na3PS4 by halogen doping: a first principles investigation, Phys. Chem. Chem. Phys. 20 (2018) 20525–20533.

[32] I.H. Chu, C.S. Kompella, H. Nguyen, Z. Zhu, S. Hy, Z. Deng, Y.S. Meng, S.P. Ong, Room-temperature all-solid-state rechargeable sodium-ion batteries with a Cl-doped Na_3PS_4 superionic conductor, Sci. Rep. 6 (2016) 33733.

[33] S. Shang, Z. Yu, Y. Wang, D. Wang, Z. Liu, Origin of outstanding phase and moisture stability in a $Na_3P_{1-x}As_xS_4$ Superionic conductor, ACS Appl. Mater. Interfaces 9 (2017) 16261–16269.

[34] Y. Hibi, N. Tanibata, A. Hayashi, M. Tatsumisago, Preparation of sodium ion conducting Na_3PS_4–NaI glasses by a mechanochemical technique, Solid State Ionics 270 (2015) 6–9.

[35] N. Tanibata, K. Noi, A. Hayashi, M. Tatsumisago, Preparation and characterization of $Na_3PS_4–Na_4GeS_4$ glass and glass-ceramic electrolytes, Solid State Ionics 320 (2018) 193–198.

[36] A. Pradel, N. Kuwata, M. Ribes, Ion transport and structure in chalcogenide glasses, Jour. of Physics: Condensed Matter 15 (2003) S1561–S1571 J. Phys. Condens. Matter.

[37] Y. Kim, J. Saienga, S.W. Martin, Preparation and characterization of germanium oxy-sulfide GeS2–GeO2 glasses, J. Non-Cryst. Solids 351 (2005) 1973–1979.

[38] Y. Kim, S.W. Martin, Ionic conductivities of various GeS2-based glasses prepared by melt-quenching and mechanical milling methods, Solid State Ionics 177 (2006) 2881–2887.

[39] A. Pradel, C. Rau, D. Bittencourt, P. Armand, E. Philippot, M. Ribes, Mixed glass former effect in the system $0.3Li_2S-0.7\,[(1-x)\,SiS_2-xGeS_2]$: a structural explanation, Chem. Mater. 10 (1998) 2162–2166.

[40] M. Schuch, C.R. Muller, P. Maass, S.W. Martin, Mixed barrier model for the mixed glass former effect in ion conducting glasses, Phys. Rev. Lett. 102 (14) (2009) 145902.

[41] C. Bischoff, The Mixed Glass Former Effect in $0.5Na_2S + 0.5[xGeS_2 + (1 − x) PS_{5/2}]$ Glasses, (2013), p. 13205 Graduate Theses and Dissertations.

[42] . D. Watson, "Mixed Glass Former Effect of 0.5 Na_2S + $0.5[xSiS_2 + (1-x) PS_{5/2}]$ and 0.67 Na_2S + $0.33[xSiS_2 + (1-x) PS_{5/2}]$ Glass Systems" (2017). Graduate Theses and Dissertations. 16239.

[43] A. Dive, C. Benmore, M. Wilding, S.W. Martin, S. Beckman, S. Banerjee, Molecular dynamics modeling of the structure and Na^+-ion transport in Na_2S + SiS_2 glassy electrolytes, J. Phys. Chem. B 122 (30) (2018) 7597–7608.

[44] C. Bischoff, K. Schuller, M. Haynes, S.W. Martin, Structural investigations of $yNa_2S + (1−y)PS_{5/2}$ glasses using Raman and infrared spectroscopies, J. Non-Cryst. Solids 358 (2012) 3216–3222.

[45] J. VandeVondele, M. Krack, F. Mohamed, M. Parrinello, T. Chassaing, J. Hutter, QUICKSTEP: fast and accurate density functional calculations using a mixed Gaussian and plane waves approach, Comput. Phys. Commun. 167 (2005) 103.

[46] J. Hutter, M. Iannuzzi, F. Schiffmann, J. VandeVondele, cp2k: atomistic simulations of condensed matter systems, WIREs Comput Mol Sci 4 (2014) 15–25.

[47] J. VandeVondele, J. Hutter, Gaussian basis sets for accurate calculations on molecular systems in gas and condensed phases, J. Chem. Phys. 127 (2007) 114105.

[48] S. Goedecker, M. Teter, J. Hutter, Separable dual-space Gaussian pseudopotentials, Phys. Rev. B 54 (1996) 1703.

[49] M. Montorsi, M.C. Menziani, C. Leonelli, A.N. Cormack, The sodium-aluminosilicate glasses: a molecular dynamic study, Mol. Eng. 8 (1998) 427.

[50] L.V. Woodcock, C.A. Angell, P. Cheeseman, Molecular dynamics studies of the vitreous state: simple ionic systems and silica, J. Chem. Phys. 65 (1976) 1565.

[51] M.J.D. Rushton, Simulations of Glass and Ceramic Systems for Nuclear Waste Applications, (2006) (Doctoral dissertation).

[52] M.C. Wilding, C.J. Benmore, Chapter 12: structure of glasses and melts in "neutron scattering in earth sciences", in: H.-K. Wenk (Ed.), Reviews in Mineralogy and Geochemistry, vol. 63, 2006, pp. 375–381.

[53] C.J. Benmore, Mario Affatigato (Ed.), X-ray Diffraction from Glass. Book Chapter 6 in Modern Glass Characterization, John Wiley and Sons, 978-1-118-23086-2, 2015, pp. 241–270.

[54] M. Montorsi, M.C. Menziani, C. Leonelli, A.N. Cormack, The sodium-aluminosilicate glasses: a molecular dynamic study, Mol. Eng. 8 (1998) 427.

[55] R. Christensen, G. Olson, S.W. Martin, Ionic conductivity of mixed glass former 0.35 $Na_2O + 0.65$ [x $B_2O_3 + (1 - x) P_2O_5$] glasses, J. Phys. Chem. B 117 (2013) $16577 - 16586$.

[56] D.K. McElfresh, D.G. Howitt, Activation enthalpy for diffusion in glass, J. Am. Ceram. Soc. 69 (10) (1986) C237–C238.

[57] M. Nose, A. Kato, A. Sakuda, A. Hayashi, M. Tatsumisago, Evaluation of mechanical properties of Na_2S–P_2S_5 sulfide glass electrolytes, J. Mater. Chem. A 3 (2015) 22061.